This is a preprint, the final version is subject to change, of the American Mineralogist (MSA)
Cite as Authors (Year) Title. American Mineralogist, in press.
(DOI will not work until issue is live.) DOI: http://dx.doi.org/10.2138/am-2017-6059

Revision 2

The nanocrystalline structure of basaluminite, an aluminum hydroxide sulfate from acid mine drainage

Sergio Carrero[a,*], Alejandro Fernandez-Martinez[b,c], Rafael Pérez-López[a], Daniel Lee[d,e], Giuliana Aquilanti[f], Agnieszka Poulain[g], Alba Lozano[h], José-Miguel Nieto[a]

[a] Department of Earth Sciences, University of Huelva, Campus 'El Carmen', 21071, Huelva, Spain

[b] CNRS, ISTerre, F-38041 Grenoble, France

[c] Université Grenoble Alpes, ISTerre, F-38041 Grenoble, France

[d] Université Grenoble Alpes, INAC, F-38000 Grenoble, France

[e] CEA, INAC, F-38000 Grenoble, France

[f] Elettra-Sincrotrone Trieste, s.s. 14 km 165.3, 34149 Basovizza. Trieste, Italy

[g] ESRF, The European Synchrotron, 71 Avenue des Martyrs, Grenoble, 38000, France

[h] Institute of Environmental Assessment and Water Research (IDAEA-CSIC). Jordi Girona 18, 08034 Barcelona, Spain

Version to be submitted to American Mineralogist, 28 December, 2016

[*]Corresponding author. Tel.: +34-95-921-9682; fax: +34-95-921-9810

E-mail address: sergio.carrero@dgeo.uhu.es (S. Carrero)

This is a preprint, the final version is subject to change, of the American Mineralogist (MSA)
Cite as Authors (Year) Title. American Mineralogist, in press.
(DOI will not work until issue is live.) DOI: http://dx.doi.org/10.2138/am-2017-6059

Abstract

Basaluminite is a poorly-crystalline aluminum hydroxysulfate that precipitates in waters affected by acid mine drainage (AMD) and in acid sulfate soils (ASS). Its ability to sequester potentially toxic elements, such as Cu and As, makes it an important component of these systems, with strong environmental implications. Although it was initially described as a mineral, basaluminite is now considered a nanoscale variety of felsöbányaite, a rare mineral. In the present study, chemical analyses of natural and synthetic basaluminites are combined with data from advanced nanoscale characterization techniques such as high-energy X-ray diffraction (HEXD) and their corresponding Pair Distribution Function (PDF) analysis, extended X-ray absorption fine structure (EXAFS) and solid-state nuclear magnetic resonance (ssNMR) spectroscopy. X-ray scattering data are analyzed with reverse Monte Carlo (RMC) modeling in order to obtain an atomistic representation of the disorder presents in this nanomineral. Sulfur K-edge EXAFS results show that sulfate is coordinated to the aluminum-octahedral framework of basaluminite mainly through outer-sphere ligands, though the existence of inner-sphere ligands seems to be slightly significant in synthetic samples. PDF analyses show that both synthetic and natural basaluminites have identical short-range order, with ~1.2 nm coherent domain size, and share structural characteristics with felsöbányaite. Interestingly, ^{27}Al ssNMR reveals the presence of, respectively, ~1% and 5% of tetrahedral and pentahedral coordinations. RMC models of basaluminite highlight the presence of structural point defects. The understanding of this nanocrystalline character has important implications in terms of the reactivity of this nanomineral in AMD and ASS and its role as scavenger of potentially toxic element (e.g. As and Se). The lack of correlation between the spatial and temporal occurrence of basaluminite and felsöbányaite suggests that the similarities between both mineral structures could be fortuitous. These findings highlights the need for further researches on previously-considered amorphous using advanced characterization techniques in order to assess their potential re-classification as nanominerals or mineral nanoparticles.

Keywords: basaluminite, felsöbányaite, structure, PDF, EXAFS, NMR.

1. Introduction

Hydrobasaluminite ($Al_4(OH)_{10}(SO_4)\cdot 34H_2O$) and basaluminite ($Al_4(OH)_{10}(SO_4)\cdot 5H_2O$) are the names given to the whitish precipitates formed in streams affected by acid mine drainage (AMD) and in acid sulfate soils (ASS) with high aluminum and sulfate concentrations, when the solution pH values are around 4.5 (Bannister and Hollingworth 1948; Hollingworth and Bannister 1950; Adams and Rawajfih 1977; Nordstrom 1982; Bigham and Nordstrom 2000). The progressive pH increase due either to mixing of AMD with pristine water or to alkaline addition in AMD treatment systems leads to solution oversaturation with respect to Al-hydroxysulfate phases, and to the formation of this poorly-crystalline precipitate. Jurbanite and alunite are other observed Al-phases in the 3-7 pH range, depending on the sulfate activity, although the metastable character of hydrobasaluminite kinetically favors its precipitation (Nordstrom 1982; Caraballo et al. 2011; Sánchez-España et al. 2011). These phases have important environmental implications because their precipitation supposes the main mechanisms controlling Al concentration. In parallel, their high surface area and positive charge in acid waters provide high affinity to potentially hazardous elements (e.g. As and Cu) present in basins impacted by AMD and in ASS (Nordstrom and Alpers 1999; Bigham and Nordstrom 2000; Carrero et al. 2015). Aluminum phases have been less studied than Fe-phases (i.e. schwertmannite, jarosite and goethite) in these environments because: (i) Fe-bearing phases precipitate at lower pH value, removing As and other toxic elements prior to the formation of Al-phases (Bigham and Nordstrom 2000; Sánchez-España et al. 2006), and (ii) Al-phases show lower crystallinity than Fe-phases, which makes their structural characterization further difficult (Adams and Rawajfih 1977; Bigham and Nordstrom 2000; Caraballo et al. 2015).

Both hydrobasaluminite and basaluminite were first described by Bannister and Hollingworth (1948) as a white plastic clay-like mineral with a variable water content. In that study, both phases were characterized with conventional X-ray techniques, showing well-defined crystalline diffraction patterns that are not congruent with a nanomineral phase. The chemical composition reported was similar to the stoichiometry of felsöbányaite, ($Al_4(OH)_{10}(SO_4)\cdot 5H_2O$). Later, Brydon and Singh (1969) observed that hydrobasaluminite irreversibly dehydrated to form basaluminite in a few days under atmospheric conditions, indicating that hydrobasaluminite was a less stable phase, being only preserved as a suspension in water. In addition, that study showed that basaluminite precipitated in the presence of clay minerals and displayed a more crystalline structure. The fact that these early studies reported diffraction

77 patterns of well-crystallized materials, and the widespread presence of clay minerals in these
78 environments, could suggest that the first identifications of basaluminite were not precise enough, and
79 that a mixture of basaluminite and clay was actually the observed mineral. More recent studies of
80 basaluminite have reported diffraction patterns with very broad peaks that are difficult to identify if other
81 crystalline phases are present in the sample (Nordstrom 1982; Bigham and Nordstrom 2000; Sánchez-
82 España et al. 2011; Carrero et al. 2015). Adams and Rawajfih (1977) showed that an Al-bearing
83 amorphous precipitate with similar composition to basaluminite occurred in streams affected by acid
84 waters, which aged to alunite and to 'crystalline basaluminite' depending upon the aging conditions. The
85 unit cell parameters of an aged precipitate were reported by Clayton (1980) from indexed X-ray powder
86 patterns, and a first structure was proposed containing octahedral Al layers with sulfate ions and variable
87 water content in the interlayer space. More recently, Farkas and Pertlik (1997) reported a structure for
88 both basaluminite and felsöbányaite, defining basaluminite as a nanoscale version of the mineral
89 felsöbányaite. However, as mentioned above, basaluminite occurs in streams affected by AMD and in
90 ASS and shows an amorphous-like X-ray pattern (Nordstrom 1982; Bigham and Nordstrom 2000;
91 Sánchez-España et al. 2011; Carrero et al. 2015). Therefore, the amorphous aluminum precipitate
92 described by Adams and Rawajfih (1977) matches well with the description of basaluminite as a non-
93 crystalline material, whereas the re-crystallized phase studied by earlier authors could be felsöbányaite.
94 This fact led to the International Mineralogical Association (IMA) to discredit basaluminite as a mineral,
95 although, interestingly, hydrobasaluminite is still considered as a valid mineral species (a status
96 'grandfathered' from earlier works before the instauration of the IMA). This historical confusion about
97 the nature of basaluminite and hydrobasaluminite, and their (lack of) relation with felsöbányaite clearly
98 deserves a thorough study. To our knowledge, felsöbányaite has never been reported in AMD or ASS
99 systems, and it is actually considered as a rare mineral. Here, we aim to shed some light on the nanoscale
100 characteristics of basaluminite formed in AMD with the hope to clarify its nature and possible re-
101 classification as a nanomineral species.

102 Caraballo et al. (2015) discussed in a recent paper the difficulties related to the identification of
103 poorly-crystalline precipitates as minerals. As described above, the case of basaluminite is paradigmatic:
104 even though it was described as a mineral earlier after its discovery, its diffraction pattern lacks clearly
105 defined peaks (Sánchez-España et al. 2011; Carrero et al. 2015). Usually, this would have been enough to
106 classify it as an amorphous material. However, as discussed by Caraballo et al. (2015), the use of

advanced characterization techniques for the study of *a priori* amorphous precipitates could facilitate the identification of nanocrystalline structural motifs that are not detectable using conventional techniques. In particular, the use of high-resolution Transmission Electron Microscopy (TEM) or of Pair Distribution Function (PDF) analyses of the short-range order have allowed to identify nanocrystallinity as well as amorphous regions in complex natural phases such as schwertmannite, and to propose periodic crystal structures for disordered phases such as ferrihydrite (Drits et al. 1993; Michel et al. 2007; Fernandez-Martinez et al. 2010; French et al. 2012). In the present work, using a combination of spectroscopic and scattering techniques we show that, in spite of its amorphous diffraction pattern, basaluminite can be described as a disordered, defective version of nanocrystalline felsöbányaite. Because basaluminite plays an important role in the metals behavior in areas affected by AMD and in ASS, these results are necessary for a better understanding of contaminant pathways in these systems.

2. Materials and methods

2.1. Solid samples

Three types of aluminum-bearing samples were studied: natural felsöbányaite, and synthetic and natural basaluminites. A sample of natural felsöbányaite from Felsöbánya (Romania) was obtained from a private collection. Natural basaluminite was obtained by slow titration under continuous stirring of an AMD solution from the Perrunal abandoned mine (Iberian Pyrite Belt, SW Spain) using a 0.01 mol L^{-1} $Ca(OH)_2$ solution, as described by Carrero et al. (2015). The precipitate was washed several times with deionized water to dissolve the co-precipitated gypsum. Synthetic basaluminite was prepared by drop-by-drop addition of 214 mL of a 0.015 mol L^{-1} $Ca(OH)_2$ solution to 30 mL of 0.05 mol L^{-1} $Al_2(SO_4)_3 \cdot 18H_2O$ with continuous stirring, according to the method described by Prietzel and Hirsch (1998). Each solid sample was freeze-dried to complete dryness using a VirTis Benchtop freeze-dryer (Hucoa-Erlöss, Spain). After drying, the samples were digested in aqua regia and stored in plastic vials for further chemical analysis.

2.2 Analytical techniques

The samples from solid digestions were analyzed for Al and S by inductively coupled plasma atomic emission spectrometry (ICP-AES; Thermo Jarrel-Ash) in the laboratories of the IDAEA (CSIC) in Barcelona. Detection limits were $2.6 \cdot 10^{-3}$ mmol L^{-1} for Al and $1.6 \cdot 10^{-2}$ mmol L^{-1} for S, and the analytical error was lower than 5%. Thermo-gravimetric analyses (TGA) were performed at the CERMAV (Univ. Grenoble Alpes, France) to determine the water content of basaluminite and felsöbányaite samples from weight loss *vs*. temperature curves using a TGA92-12 SETARAM, with a N_2 flow of 1.8 l/h, between room temperature and 690 ºC, with a rate of temperature increase of 9.8 ºC min^{-1} under nitrogen flow.

HEXD experiments were performed at the ID31 beamline of the European Synchrotron Radiation Facility (ESRF, Grenoble, France). Powder samples were loaded into polyimide (Kapton) capillaries. Sample and background measurements were carried out at room temperature in a Q-range of 0-25 $Å^{-1}$. Incident X-rays had an energy of 69.5 keV (λ = 0.1784 Å), calibrated using a CeO_2 standard (NIST 679b). The 2D-images collected by the flat panel Perkin Elmer 2D detector were corrected and integrated using Fit2D (Hammersley et al. 1996). Structure factors, S(Q), and PDF, were obtained using the PDFGetX3 software (Farrow et al. 2009). In addition, partial PDFs of felsöbányaite were calculutated in order to identify the different atom pairs in the PDF. More information about partial PDF can be found in the section S1 of the Supporting Information (SI).

Sulfur K-edge EXAFS data for natural and synthetic basaluminite were collected at the beamline "XAFS" of synchrotron Elettra (Trieste, Italy). Spectra were collected at the sulfur K-edge (2485 eV) in fluorescence mode at a temperature of 100 K. The sample was ground and suspended under ultrasonic vibration in 30 mL of cyclohexane. Immediately, the suspension was filtered through a 0.1 µm cellulose membrane filter and dried at room temperature. EXAFS data were taken in a range from 2300 to 3220 eV with 0.2 eV step size at the edge region. EXAFS data reduction and fitting were performed using the Athena and Artemis software of the IFFEFIT package (Ravel and Newville 2005). Structural models of sulfate in basaluminite were constructed using the felsöbányaite structure proposed by Farkas and Pertlik (1997). Debye-Waller factors, interatomic distances, coordination numbers and Fermi energy levels were fitted using a least-square refinement algorithm. Statistical F-tests (Joyner et al. 1987; Michalowicz et al. 1999) were applied to determine the statistical significance of different tested hypotheses involving different numbers of shells added to the models. Only those models that improved the fit between theoretical and experimental EXAFS at the 90% level of confidence were selected.

Solid-state NMR spectra were recorded using a Bruker Avance II spectrometer operating at 9.4 T, corresponding to a ^{27}Al Larmor frequency of 104.2 MHz, equipped with a triple-resonance 3.2 mm magic-angle spinning (MAS) probe. ^{27}Al MAS NMR experiments were recorded at approximately 300 K, using a hard and short (0.5 μs) radiofrequency pulse (ensuring uniform excitation), a MAS rate of 20 kHz, an experimental repetition delay of 5 s and required approximately only 20 min of cumulative acquisition. The spectral width was 100 kHz and the free induction decay (FID) was measured for 3.2 ms, during which 100 kHz SPINAL-64 heteronuclear decoupling (Fung et al. 2000) was applied. ^{27}Al *z*-filtered multiple-quantum magic-angle spinning (MQMAS) spectra (Amoureux et al. 1996) were recorded under the same experimental conditions as for the ^{27}Al MAS NMR experiments except 792 co-added transients were acquired for each of 64 indirect dimension points, using an experimental repetition delay of 0.5 s, resulting in a total experimental time of ~14 h. The spectral width in the indirect dimension was 60 kHz, triple quantum excitation and reconversion were achieved using pulses of 6.0 and 1.6 μs, respectively, and a central-transition-selective "read"-pulse of 8 μs was applied before signal detection.

2.3 Rietveld refinement and Reverse Monte Carlo structural models

Basaluminite structural models were constructed from Reverse Monte Carlo simulations, using different modified felsöbányaite structures (Farkas and Pertlik 1997) as starting points. Prior to that, the crystal structure of felsöbányaite was refined by the Rietveld method with the FullProf suite programs (Rodríguez-Carvajal 1993) using a powder X-ray diffraction pattern of natural felsöbányaite. The diffraction pattern was collected on a Siemens D5000 diffractometer in Bragg-Brentano geometry, equipped with a theta-theta goniometer with a rotating sample holder. The patterns were collected using Cu kα_1 ($\lambda_{k\alpha1}$ = 1.5406 Å) and kα_2 ($\lambda_{k\alpha2}$ = 1.5444 Å) radiation in the range 2θ = 0-70° with a step size of 0.04° and a counting time of 6 s per step. Specific constraints were applied during the Rietveld refinement to consider the sulfate molecule as a rigid body. The results obtained by Rietveld analysis are showed in Table S1 and Figure S1 of the SI.

A single RMC move involves the random displacement of a number of atoms, which modifies the calculated structure factor, S(Q), and the PDF of the model structure. Then, a χ^2 is calculated for all the points *i* of the S(Q) and G(r):

$$\chi^2 = \left\{ \Sigma_i \left[S(Q_i)_{exp} - S(Q_i)_{calc} \right]^2 + \Sigma_i \left[G(r_i)_{exp} - G(r_i)_{calc} \right]^2 \right\} / \sigma^2 \qquad \text{Eq. 1}$$

where σ is a weight factor. RMC moves are automatically accepted when χ^2 is decreased, and are accepted with a probability P = exp ($-\Delta\chi^2/2$) when χ^2 increases. Atom displacements are rejected if they violate the close-contact distances between atoms (see Table S2 of the SI). Bond lengths (S-O) and angles (O-S-O) of the sulfate molecules were constrained to restrict their deformation to less than 20%. Details of the RMC simulation are indicated in section S2 of the SI.

3 Results

3.1 Chemical characterization

The stoichiometry of both natural basaluminite [$Al_4(OH)_{9.20}(SO_4)_{1.40}\cdot 4.77H_2O$] and synthetic basaluminite [$Al_4(OH)_{9.02}(SO_4)_{1.49}\cdot 4.56H_2O$] was characterized by a higher sulfate content than the chemical formula reported by Hollingworth and Bannister (1950) and Farkas and Pertlik (1997), with only one sulfate per four aluminum atoms (see Table S3 of the SI).

TGA analyses of natural felsöbányaite, and natural and synthetic basaluminites are shown in Figure S2 of the SI. TGA data of felsöbányaite showed three different weight losses of 8.21%, 6.30% and 17.2% between 50 ºC and 120 ºC, 130 ºC and 185 ºC, and 270 ºC and 340 ºC, respectively (Fig. S2). The first and second steps (~14.5 wt.%) are interpreted as corresponding to loosely bound physisorbed and structural H_2O (Brydon and Singh 1969). The third step (~17.2 wt.%) was associated with the release of structural OH. These weight losses are close to those found for the structure reported by Farkas and Pertlik (1997). In contrast, TGA data of both natural and synthetic basaluminites produced a unique large sigmoidal-like water desorption and decomposition step between 90 ºC and 300 ºC, with associated weight losses of 34.5 wt.% and 34.4 wt.%, respectively. Following this period, the sample weight was constant with a slight decreasing tendency between 300 ºC to 600 ºC (Fig. S2). The weight loss observed in both solids was associated with the vaporization of physisorbed H_2O and of structural OH/H_2O. Dehydration reactions can be described by Eqs. 2 and 3 for natural and synthetic basaluminites, respectively:

$$Al_4(OH)_{9.20}(SO_4)_{1.40}\cdot 4.77H_2O \rightarrow Al_4O_{4.60}(SO_4)_{1.40} + 9.37H_2O \quad \text{Eq. 2}$$

$$Al_4(OH)_{9.02}(SO_4)_{1.49}\cdot 4.56H_2O \rightarrow Al_4O_{4.51}(SO_4)_{1.49} + 9.07H_2O \quad \text{Eq. 3}$$

The fact that felsöbányaite reveals three well-differentiated weight losses and basaluminite shows just one is interpreted as being due to the structural disorder present in basaluminite. Moreover, the similarity between the curves of natural and synthetic basaluminites suggests that, even though the basaluminite structure is disordered, water in both structures shares similar positions.

3.2 Structural characterization

3.2.1 High-energy X-ray diffraction

Structure factors, S(Q), obtained from the diffraction patterns of the three samples are shown in Figure 1a. Lab-based X-ray diffraction patterns of felsöbányaite and basaluminite are showed in Figure S3, showing low-angle peaks indicative of mesoscale ordering of basaluminite domains, similarly to the periodic order of the layered felsobanyaite structure along the [10-1] direction. S(Q)s of natural and synthetic basaluminites present similar characteristics, with the regions of maximum peak intensity and diffuse scattering distributed along Q similar to felsöbányaite, suggesting similar structural characteristics. As expected, the structure factor of both basaluminite samples lacks any well-defined diffraction peak, suggesting a poorly-crystalline material (Fig. 1a).

PDFs of natural and synthetic basaluminites and natural felsöbányaite are shown in Figure 1b. In addition, calculated partial PDFs of felsöbányaite (Farkas and Pertlik 1997) (Al-Al, Al-O, Al-S, S-S, S-O and O-O atom pairs) are displayed in Figure S4 of the SI. PDFs of synthetic and natural basaluminites reveal that the synthesis process yields nanoparticles with very similar local order. Slight differences in peak intensity and width could probably be related to the presence of impurities in the structure of the natural samples (see solution compositions in Table S3). The intensity decay along *r* was fitted with an envelope function reproducing particles of spherical shape (Gilbert 2008), considering as well the instrumental resolution effect determined previously with the CeO_2 standard (Toby and Egami 1992). Natural and synthetic samples of basaluminite showed an identical coherent domain size of about 1.2 nm, while the coherent domain size obtained for the felsöbányaite sample was in the range of 4-5 nm. PDFs of both felsöbányaite and basaluminite exhibited similar structural features in the region between 1 and 6 Å, but with significant variations in peak intensities and width (Fig. 1b). Both basaluminite and felsöbányaite PDFs were compared in order to identify similarities and to associate individual peaks to interatomic

distances using the calculated partial PDFs of felsöbányaite. The position of the first peak at 1.45 Å corresponds to the S-O distance in the sulfate tetrahedron, whereas the second peak at 1.88 Å is attributed to the Al-O distance in the aluminum octahedron. The peak at 3 Å corresponds to the superposition of Al-Al and O-O distances, where the Al-Al distance corresponds to edge-sharing aluminum octahedra and the O-O distance is related to consecutive oxygen atoms in the octahedra. The next three peaks (at 4, 4.8 and 6 Å) are mainly due to Al-O distances. Beyond r = 6 Å, the PDF of basaluminite shows a noise level (Fourier truncation error) comparable to the signal.

3.2.2 Solid-state nuclear magnetic resonance

^{27}Al MAS and ^{27}Al MQMAS NMR spectra are shown in Figures 2 and 3, respectively. Aluminum in amorphous and mineral phases has been observed in 4-, 5- and 6-coordination states [Al(IV), Al(V) and Al(VI)], where Al(IV), Al(V) and Al(VI) are represented by ^{27}Al MAS NMR peaks between +55 and +85 ppm, +30 and +41 ppm, and +0 and +15 ppm, respectively (Kirkpatrick and Phillips 1993). Both natural and synthetic basaluminites showed similar Al-coordination, where Al(VI) was the most abundant coordination, characterized by a broad peak, highlighting the presence of a range of Al-O-Al bond angles (i.e., high degree of structural disorder). Interestingly, Al(V) and Al(IV) also occur in the structure but to a much lesser extent, about 5% and 1%, respectively (Figs. 2 and 3a). These Al-coordination states have been previously reported in white precipitates collected in systems affected by acid water (Kim 2015). ^{1}H NMR data (not shown) indicated the presence of physisorbed H_2O as well as Al-OH hydroxyl groups. There is no evidence of Al(IV) or Al(V) coordination in felsöbányaite (Figs. 2 and 3b). Although felsöbányaite contains only Al(VI) coordination like gibbsite, the 27Al MAS NMR spectrum of which is shown in Fig. 2 for comparison, it is evidently less well ordered owing to the larger linewidth of the corresponding NMR peak. Moreover, the Al(VI) coordination of both natural and synthetic basaluminites are even less ordered, according to the broader Al(VI) peaks (Figs. 2 and 3), with the natural sample being the most amorphous.

3.2.3 Reverse Monte Carlo models

The qualitative analysis of the PDF data and the similarities in the Al(VI) coordinations found by ssNMR suggest that the basaluminite structure seems to have similar features to that of felsöbányaite, though with non-negligible distortions, as suggested by Farkas and Pertlik (1997). Based on this observation, and in order to develop an atomistic structural model of basaluminite that matches the diffraction data and the PDF analysis, a RMC refinement strategy was followed.

The evolution of the χ^2 agreement parameter of the models used (*fels1*, *fels2* and *fels3,* see details in the section S2 of the SI) is shown in Figure S5 of the SI. The three structures show similar final χ^2 values, indicating that the three of them provide equally good representation of the scattering data. Even though longer simulations provided better agreement, a choice was made to stop RMC simulations once the χ^2 started to show a plateau; RMC simulations that were run for a longer time (larger number of steps), provided similar χ^2 values, but showed higher structural disorder.

Differences between experimental and modeled S(Q) and G(r) are displayed in Figure 4. Views of the atomistic structure are shown in Figure S6 of the SI. The model kept the octahedral Al layer structure, with only slight distortions. Sulfate and water molecules placed in the interlayer space were slightly displaced from their original positions. However, the contribution of these molecules to the total PDF and to the scattering was negligible (Figs. S4 and 4), and therefore no unambiguous information about their positions can be reported.

3.2.4 Sulfur K-edge EXAFS

Sulfur K-edge EXAFS from synthetic and natural basaluminites, and the parameters of the structural models achieved are shown in Figure 5 and Table 1. Results from natural basaluminite reveal the presence of one shell at 1.453 ± 0.002 Å, which is attributed to the S-O distance (Fig. 5). This peak is consistent with an undistorted sulfate tetrahedron with coordination number of 5.119 (± 0.051). Three different models were considered during the fitting process: (i) a sulfate in an outer-sphere position (just one shell); (ii) a surface complex with a monodentate ligand; and (iii) a surface complex with a bidentate binuclear ligand on aluminum octahedral layers. A model where sulfate is forming an outer-sphere location yields the best fit (Table 1) and a 75% confidence in the F-test (see all parameters used for the F-tests in Tables S4, S5 and S6 in the SI), which is in agreement with the localization of sulfate in felsöbányaite (Farkas and Pertlik 1997). On the other hand, S K-edge EXAFS in synthetic basaluminite

shows that sulfate is retained by bidentate binucleate inner-sphere covalent ligands, where a double shell is identified with peaks located at 1.458 ± 0.003 Å and 3.017 ± 0.033 Å. These peaks are associated to S-O and S-Al distances with coordination number of 4.583 ± 0.051 and 2.00 (fixed value), respectively (Fig. 5 and Table 1). The F-test values obtained for these models indicate that the bidentate binuclear inner-sphere is the best fit, where the confidence level was 60% (Table S6). The confidence levels obtained in both F-test studies are close to or less than minimum necessary, indicating that both models are possible and that the second shell is near the limit of detection.

4 Discussion

4.1 Sulfate and water environments in basaluminite

The higher sulfate contents observed in both natural and synthetic basaluminites with respect to the chemical composition reported for felsöbányaite (Hollingworth and Bannister 1950; Farkas and Pertlik 1997) could be related to the nanocrystalline, defective structure of basaluminite and its larger surface area. This difference in oxyanion content by nanomineral phases has been reported in other precipitates present in AMD and ASS (e.g., schwertmannite; Bigham et al., 1994). The different sulfate structural positions observed in natural and synthetic basaluminites could be associated with the higher sulfate concentration in solution during the synthesis of basaluminite, resulting in a higher proportion of adsorbed sulfate. In fact, the sulfate content is slightly higher in synthetic than in natural basaluminite (Al/S = 2.86 and 2.68 in natural and synthetic basaluminites, respectively). EXAFS results and statistical F-test analysis indicated that sulfate shows a bidentate coordination with the Al framework in synthetic basaluminite, though the statistical significance of this result is near the limit of acceptable confidence. Actually, both spectra are very similar, with mainly one frequency associated to the S-O distance. The presence of inner-sphere sulfate in synthetic basaluminite could be explained by the higher sulfate concentration in these samples, and therefore the higher probability that some sulfate can adopt different bonding environments. Most sulfate is retained in basaluminite by outer-sphere ligands, such as those present in the felsöbányaite structure (Farkas and Pertlik 1997).

A previous study has reported a detailed investigation of sulfate bonding environment in schwertmannite, another poorly crystalline mineral from AMD and ASS. Different local environments are

described as a function of the level of hydration of the sample. In air-dried samples, reactive singly-Fe coordinated hydroxyl groups react through a ligand exchange process with sulfate, forming inner-sphere complexes. On the other hand, sulfate in wet samples is mainly coordinate in outer-sphere position (Wang et al. 2015). A similar behavior could be present in basaluminite. Both, natural and synthetic samples present a high defective Al-framework, but the lower water content and the impossibility to form water mediated H-bonding, could lead to the presence of inner-sphere ligands in synthetic basaluminite.

Finally, the unique large sigmoidal-like water desorption step observed in TGA data indicates that the physisorbed water and hydroxyl groups in both natural and synthetic basaluminites present similar disordered environments with non-well-defined structural positions, as compared to felsöbányaite (Fig. S2). However, no further information about the water positions in the structure could be obtained due to their very low X-ray scattering weight factor, resulting in a negligible contribution to the total PDF.

4.2 Aluminum framework

The high structural correlation observed between basaluminite and felsöbányaite in the first 6 Å of the PDF and the good fit obtained with RMC with only slight distortions of the felsöbányaite structure indicate that basaluminite can be described as a mineral nanoparticle. Two structural models were considered to explain the origin of this disorder that match well the observed Al/S ratio: (i) a structure formed by an identical Al-framework to that of felsöbányaite, where excess sulfate was due to formation of surface complexes on the external surface, and (ii) a structure where aluminum point defects (vacancies) are present in the Al layers. RMC simulations of these two models yielded similar χ^2 values (Fig. S5), indicating that both are equally plausible. In addition, the Al-O first neighbor distances shows a distortion to lower Al-O distances (Fig. S7). The asymmetric shape can be at least partially due to the presence of Al(IV) and Al(V) coordination in basaluminite (Al(IV)-O and Al(V)-O distance in oxyhydroxide phases are in the order of 1.76 and 1.80, respectively, Kubicki 1998). It is worth noting here that the atomistic models resulting from the RMC are not to be understood as a precise, crystallographic description of the basaluminite structure. The RMC method is a statistical method, whose results should be interpreted in a statistical way. Large supercells were used in order to allow for the presence of different distortions in the short-range order region. Whether basaluminite exists as a single

nanoparticle or as an extended disordered network (gel) cannot be addressed by the local-order probes used here.

The presence of tetrahedral and pentahedral Al-coordinations in basaluminite found by ssNMR spectroscopy is an important difference between felsöbányaite and basaluminite. Different reasons can explain the presence of tetrahedral Al: (i) Al(IV) is a structural component in silicate minerals, such as feldspars and phyllosilicates (^{27}Al NMR peaks at 70 ppm in a magnetic field of 10 T; Kirkpatrick and Phillips, 1993), and basaluminite precipitation in streams affected by AMD and ASS is associated with the removal of Si from the solution (Bigham and Nordstrom, 2000). *A priori*, HEXD results found no evidence of crystalline silicate minerals, with basaluminite being the only phase present in the samples (Fig. 1). However, the presence in small proportions of a disordered aluminosilicate phase cannot be ruled out from these experiments. (ii) Al_{13} keggin ions (^{27}Al NMR peaks at 60 ppm in a magnetic field of 10 T, Kirkpatrick and Phillips, 1993), which contain one Al site in a tetrahedral coordination, have been proposed as a structural building motifs for many Al-oxyhydroxide phases (such as gibbsite, boehmite and bayerite; Jolivet et al., 2011), and it could be possible that they also participate in the precipitation process of basaluminite. Indeed, the NMR chemical shift of 60 ppm found here for Al(IV) in basaluminite matches the value found for sulfate-bearing phases formed from Al_{13} Keggin ions in the same magnetic field of 10 T (Kirkpatrick and Phillips 1993) (Figs. 2 and 3a). Additionally, the presence of Al(V) in basaluminite (~5%) is characteristic of materials with large surface areas (Kirkpatrick and Phillips, 1993), where water molecules are coordinated to surface Al(V) atoms.

4.3 Implications: On the mineral nature of nanomineral species

The lack of clearly defined peaks in the diffraction patterns, due to small coherent domain size and to the accumulation of structural defects, prevents us from defining a unit cell to describe the basaluminite structure. However, the use of the PDF method clearly shows that the average local order is not far from that of a disordered felsöbányaite nanoparticle. However, the different geological occurrences of felsöbányaite and basaluminite makes that more careful analyses need to be performed on the structure of the aged basaluminite. A couple of studies (Adams and Rawajfih, 1977 and Brydon and Singh, 1968) reported the formation of a so-called 'crystalline basaluminite' when aged in the presence of Ca-bearing solutions at 50°C. Interestingly, these conditions are similar to the ones that could be found in alkaline

403 'chalky' sedimentary environments where some of the first basaluminite occurrences were described
404 (Bannister and Hollingworth 1948; Brydon and Singh 1969; Clayton 1980). But, to the best of our
405 knowledge, felsöbányaite or 'crystalline basaluminite' have never been reported in AMD or ASS
406 environments. More studies need to be undertaken to better understand the relationship between these two
407 phases and the aging mechanisms. Performing these studies would help to clarify the status of
408 basaluminite as a single nanomineral species or as a felsöbányaite mineral nanoparticle. They will also
409 clarify the potential release of adsorbed oxyanions upon basaluminite aging, with important
410 environmental consequences in AMD-affected sites (Carrero et al. 2017).

411 This work highlights the need of careful analysis and possible revision of amorphous structures, and
412 their potential re-classification as nanominerals. Following recent discussions in the mineralogical
413 literature (Caraballo et al., 2015), this could then just be interpreted as a case where the use of advanced
414 characterization techniques allows revealing the nature of a mineral nanoparticle that would have been
415 otherwise classified as an amorphous material. The advent of advanced characterization techniques is
416 providing unprecedented structural details of disordered solids, linking some structures to already known
417 mineral phases (Hochella et al. 2008; French et al. 2012; Grangeon et al. 2017), and unraveling the
418 existence of structural defects in materials that, in some cases, provide them with functional advantages.
419 More work in this direction is needed to establish more links between the world of amorphous
420 precipitates to that of nanominerals and mineral nanoparticles.
421

Associated information

Supporting Information. The supporting information contains: 1) details of partial distribution function of felsöbányaite, indicating the equation employed in the calculations (S1); 2) details of Reverse Monte Carlos simulation (S2); 3) tables with close-contact interatomic distances and final lattice parameters obtained in RMC, the chemical results of solid digestion and the parameters and F-test results of the different models considered during the EXAFS refinement; and 4) seven figures illustrating the details of the solid phases characterization and structural simulations.

Acknowledgments

We would like to thank the Regional Government of Andalucía (Spain; P12-RNM-2260), the Spanish Ministry of Economic and Competitiveness (EMPATIA, CGL2013-48460-C2-R) and a grant from Labex OSUG@2020 (investissements d'avenir – ANR10 LABX56) for financial research support. S. Carrero was supported by a research predoctoral fellowship AP2010-2117 (Spanish Ministry of Education, Spain). R. Pérez-López also thanks the Spanish Ministry of Science and Innovation and the 'Ramón y Cajal Subprogramme' (MICINN-RYC 2011). The authors are very grateful to the ESRF (ID31 beamline) and Elettra (beamline "XAFS") personnel for their assistance during our experiment (20145106). Chemical analyses were performed at the laboratories of IDAEA (CSIC) in Barcelona. We would also like to thank Dr. Keith Putirka (Editor), Dr. David Singer (Associated Editor) and two anonymous reviewers for the comments that significantly improved the quality of the original paper.

References

Adams, F., and Rawajfih, Z. (1977) Basaluminite and alunite: A possible cause of sulfate retention by acid soils. Soil Science Society of America Journal, 41, 686–692.

Amoureux, J.-P., Fernandez, C., and Steuernagel, S. (1996) Z filtering in MQMAS NMR. Journal of Magnetic Resonance, 123, 116–118.

Bannister, F.A., and Hollingworth, S.E. (1948) Two new British minerals. Nature, 162, 565.

Bigham, J.M., and Nordstrom, D.K. (2000) Iron and aluminum hydroxysulfates from acid sulfate waters. Reviews in Mineralogy and Geochemistry, 40, 351–403.

Bigham, J.M., Carlson, L., and Murad, E. (1994) Schwertmannite, a new iron oxyhydroxysulphate from Pyhasalmi, Finland, and other localities. Mineralogical Magazine, 58, 641–648.

Brydon, J.E., and Singh, S.S. (1969) The nature of the synthetic crystalline basic aluminium sulphate as compared with basaluminite. Canadian Mineralogist, 9, 644–654.

Caraballo, M.A., Macías, F., Rötting, T.S., Nieto, J.-M., and Ayora, C. (2011) Long term remediation of highly polluted acid mine drainage: A sustainable approach to restore the environmental quality of the Odiel river basin. Environmental Pollution, 159, 3613–3619.

Caraballo, M.A., Michel, F.M., and Hochella, M.F. (2015) The rapid expansion of environmental mineralogy in unconventional ways: Beyond the accepted definition of a mineral, the latest technology, and using nature as our guide. American Mineralogist, 100, 14–25.

Carrero, S., Pérez-López, R., Fernandez-Martinez, A., Cruz-Hernández, P., Ayora, C., and Poulain, A. (2015) The potential role of aluminium hydroxysulphates in the removal of contaminants in acid mine drainage. Chemical Geology, 417, 414–423.

Carrero, S., Fernandez-Martinez, A., Perez-Lopez, R., Poulain, A., Salas-Colera, E., and Nieto, J.M. (2017) Arsenate and selenate scavenging by basaluminite: Insights into the reactivity of aluminum phases in acid mine drainage. Environmental Science & Technology, 51, 28–37.

Clayton, T. (1980) Hydrobasaluminite and basaluminite from Chickerell, Dorset. Mineralogical Magazine, 43, 931–937.

Drits, V.A., Sakharov, B.A., Salyn, A.L., and Manceau, A. (1993) Structural model for ferrihydrite. Clay Minerals, 28, 185–207.

Farkas, L., and Pertlik, F. (1997) Crystal structure determinations of felsöbányaite and basaluminite, Al4(SO4)(OH)10·4H2O. Acta Mineralogica-Petrographica, Szeged, 38, 5–15.

473 Farrow, C.L., Juhás, P., Liu, J.W., Bryndin, D., Bozin, E.S., Bloch, J., Proffen, T., and Billinge, S.J.L.
474 (2009) PDFgui user guide.
475 Fernandez-Martinez, A., Timon, V., Román-Ross, G., Cuello, G.J., Daniels, J.E., and Ayora, C. (2010)
476 The structure of schwertmannite, a nanocrystalline iron oxyhydroxysulfate. American Mineralogist,
477 95, 1312–1322.
478 French, R.A., Caraballo, M.A., Kim, B., Rimstidt, J.D., Murayama, M., and Hochella, M.F. (2012) The
479 enigmatic iron oxyhydroxysulfate nanomineral schwertmannite: Morphology, structure, and
480 composition. American Mineralogist, 97, 1469–1482.
481 Fung, B.M., Khitrin, A.K., and Ermolaev, K. (2000) An improved broadband decoupling sequence for
482 liquid crystals and solids. Journal of magnetic resonance, 142, 97–101.
483 Gilbert, B. (2008) Finite size effects on the real-space pair distribution function of nanoparticles. Journal
484 of Applied Crystallography, 41, 554–562.
485 Grangeon, S., Fernandez-Martinez, A., Baronnet, A., Marty, N., Poulain, A., Elkaïm, E., Roosz, C.,
486 Gaboreau, S., Henocq, P., Claret, F., and others (2017) Quantitative X-ray pair distribution function
487 analysis of nanocrystalline calcium silicate hydrates: a contribution to the understanding of cement
488 chemistry. Journal of Applied Crystallography, 50, 14–21.
489 Hammersley, A.P., Svensson, S.O., Hanfland, M., Fitch, A.N., and Häusermann, D. (1996) Two-
490 dimensional detector software: From real detector to idealised image or two-theta scan. High
491 Pressure Research, 14, 235–248.
492 Hochella, M.F., Lower, S.K., Maurice, P.A., Penn, R.L., Sahai, N., Sparks, D.L., and Twining, B.S.
493 (2008) Nanominerals, mineral nanoparticles, and Earth systems. Science, 319, 1631–1635.
494 Hollingworth, S.E., and Bannister, F.A. (1950) Basaliminite and hydrobasaluminite, two new minerals
495 from Northamptonshire. Journal of the Mineralogical Society, 29, 1–17.
496 Jolivet, J.-P., Chanéac, C., Chiche, D., Cassaignon, S., Durupthy, O., and Hernandez, J. (2011) Basic
497 concepts of the crystallization from aqueous solutions: The example of aluminum oxy(hydroxi)des
498 and aluminosilicates. Comptes Rendus Geoscience, 343, 113–122.
499 Joyner, R.W., Martin, K.J., and Meehan, P. (1987) Some application of statistical tests in analysis of
500 EXAFS and SEXAFS. Journal of Physics C: Solid State Physics, 20, 4005–4012.
501 Kim, Y. (2015) Mineral phases and mobility of trace metals in white aluminum precipitates found in acid
502 mine drainage. Chemosphere, 119, 803–811.

503 Kirkpatrick, R.J., and Phillips, B.L. (1993) 27Al NMR spectroscopy of minerals and related materials.
504 Applied Magnetic Resonance, 4, 213–236.
505 Kubicki, J.D. (1998) Molecular cluster models of aluminum oxide and aluminum hydroxide surfaces.
506 American Mineralogist, 83, 1054–1066.
507 Michalowicz, A., Provost, K., Laruelle, S., Mimouni, A., and Vlaic, G. (1999) F-test in EXAFS fitting of
508 structural models. Journal of synchrotron radiation, 6, 233–235.
509 Michel, F.M., Ehm, L., Antao, S.M., Lee, P.L., Chupas, P.J., Liu, G., Strongin, D.R., Schoonen, M.A.A.,
510 Phillips, B.L., and Parise, J.B. (2007) The structure of ferrihydrite, a nanocrystalline material.
511 Science, 316, 1726–1729.
512 Nordstrom, D.K. (1982) The effect of sulfate on aluminum concentrations in natural waters: Some
513 stability relations in the system Al2O3-SO3-H2O at 298 K. Geochimica et Cosmochimica Acta, 46,
514 681–692.
515 Nordstrom, D.K., and Alpers, C.N. (1999) Geochemistry of acid mine waters. (G.S. Plumlee & M..
516 Logsdon, Eds.)Society & Economic Geologists, 6A, 133–160.
517 Prietzel, J., and Hirsch, C. (1998) Extractability and dissolution kinetics of pure and soil-added
518 synthesized aluminium hydroxy sulphate minerals. European Journal of Soil Science.
519 Ravel, B., and Newville, M. (2005) ATHENA, ARTEMIS, HEPHAESTUS: Data analysis for X-ray
520 absorption spectroscopy using IFEFFIT. Journal of Synchrotron Radiation, 12, 537–541.
521 Rodríguez-Carvajal, J. (1993) Recent advances in magnetic structure determination by neutron powder
522 diffraction. Physica B: Condensed Matter, 192, 55–69.
523 Sánchez-España, J., López Pamo, E., Santofimia Pastor, E., Reyes Andrés, J., and Matín Rubí, J.A.
524 (2006) The removal of dissolved metals by hydroxysulphate precipitates during oxidation and
525 neutralization of acid mine waters, Iberian Pyrite Belt. Aquatic Geochemistry, 12, 269–298.
526 Sánchez-España, J., Yusta, I., and Diez-Ercilla, M. (2011) Schwertmannite and hydrobasaluminite: A re-
527 evaluation of their solubility and control on the iron and aluminium concentration in acidic pit
528 lakes. Applied Geochemistry, 26, 1752–1774.
529 Toby, B.H., and Egami, T. (1992) Accuracy of pair distribution function analysis applied to crystalline
530 and non-crystalline materials. Acta Cristallographica Section A, 48, 336–346.
531 Wang, X., Gu, C., Feng, X., and Zhu, M. (2015) Sulfate local coordination environment in
532 schwertmannite. Environmental Science & Technology, 49, 10440–10448.

533

534 **Figure captions**

535

536 FIGURE 1: (a) X-ray diffraction structure factor (S(Q)) and (b) PDFs of felsöbányaite (black), and
537 natural (red) and synthetic (blue) basaluminites.

538 FIGURE 2: ^{27}Al MAS NMR spectra of basaluminite, felsöbányaite and gibbsite (standard). The
539 three bands represent Al(IV)-, Al(V)- and Al(VI)-coordination. The intensity scaling is arbitrary.

540 FIGURE 3: 2D ^{27}Al MQMAS-^{27} NMR spectra of (a) basaluminite and (b) felsöbányaite.

541 FIGURE 4: Experimental (a) structure factor and (b) pair distribution function of synthetic
542 basaluminite (black) compared with those obtained from RMC with the *fels2 [2,2,2]* structure (red), and
543 the difference (green).

544 FIGURE 5: (a) K^3-weighted EXAFS spectra and (b) their Fourier transform amplitude at the S K-
545 edge of natural and synthetic basaluminites. Experimental and fitted curves are displayed in black and red
546 color, respectively.

547

548 **Table captions**

549

550 TABLE 1: Modeling parameters for S K-edge EXAFS with 100% outer-sphere coordination and
551 100%, bidentate binucleate inner-sphere ligand in natural and synthetic basaluminite, respectively.

552

This is a preprint, the final version is subject to change, of the American Mineralogist (MSA)
Cite as Authors (Year) Title. American Mineralogist, in press.
(DOI will not work until issue is live.) DOI: http://dx.doi.org/10.2138/am-2017-6059

Revise Figure 1

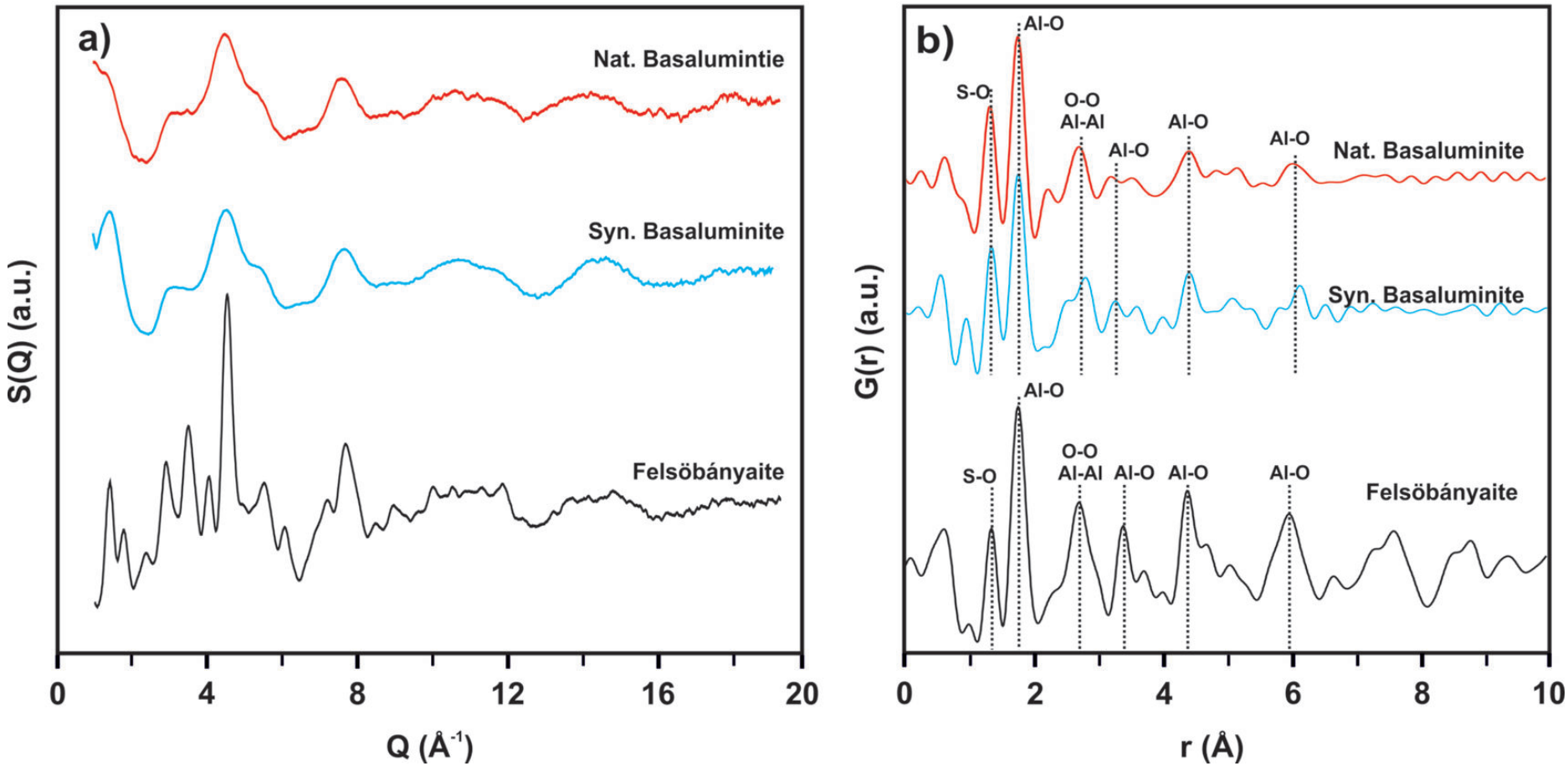

This is a preprint, the final version is subject to change, of the American Mineralogist (MSA)
Cite as Authors (Year) Title. American Mineralogist, in press.
(DOI will not work until issue is live.) DOI: http://dx.doi.org/10.2138/am-2017-6059

Figure 2

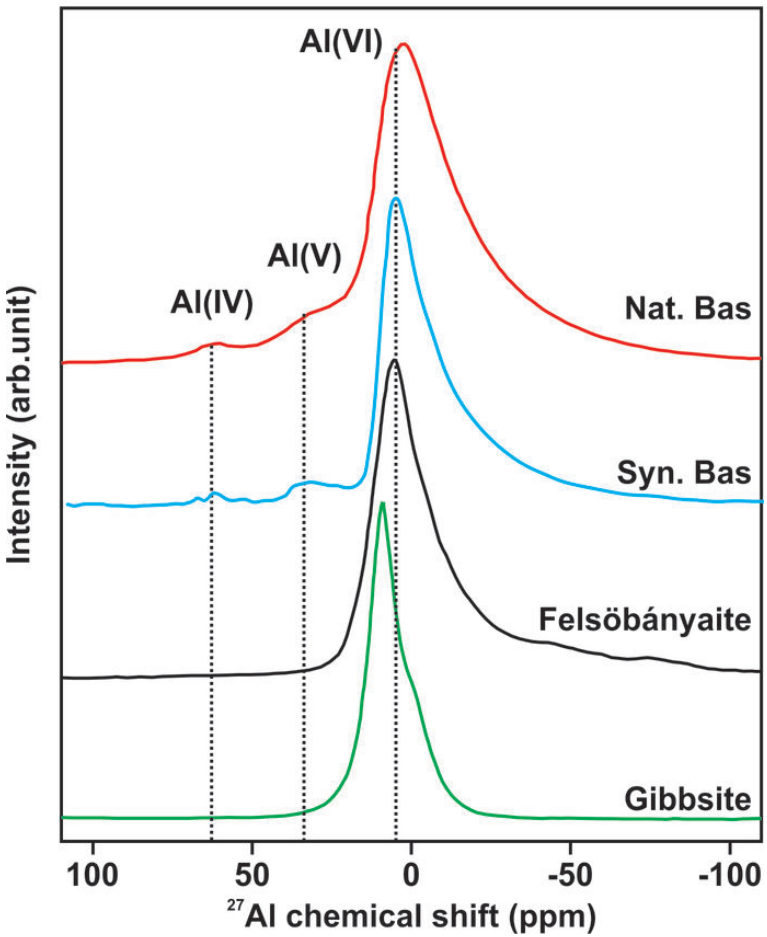

This is a preprint, the final version is subject to change, of the American Mineralogist (MSA)
Cite as Authors (Year) Title. American Mineralogist, in press.
(DOI will not work until issue is live.) DOI: http://dx.doi.org/10.2138/am-2017-6059

Figure 3

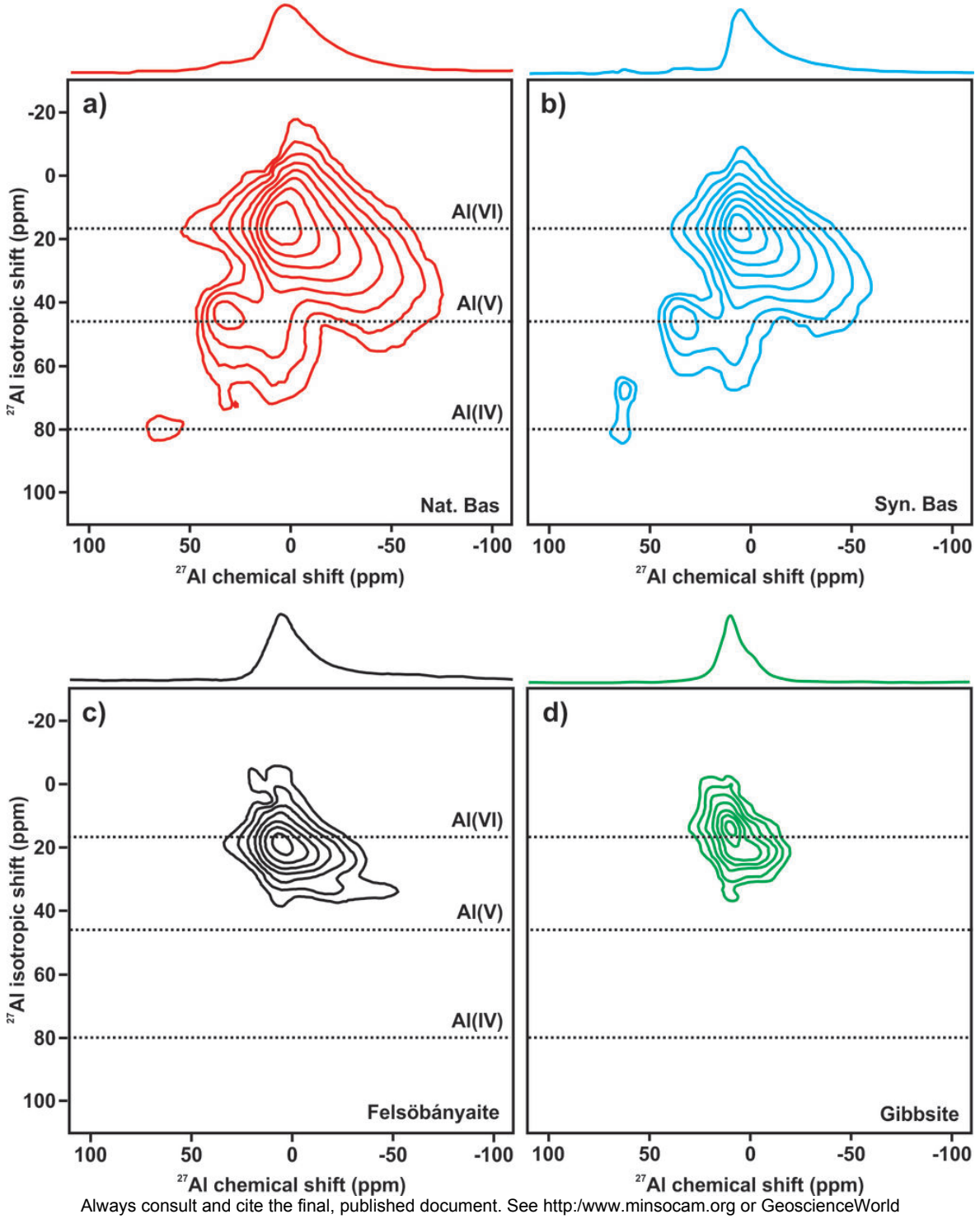

This is a preprint, the final version is subject to change, of the American Mineralogist (MSA)
Cite as Authors (Year) Title. American Mineralogist, in press.
(DOI will not work until issue is live.) DOI: http://dx.doi.org/10.2138/am-2017-6059

Figure 4

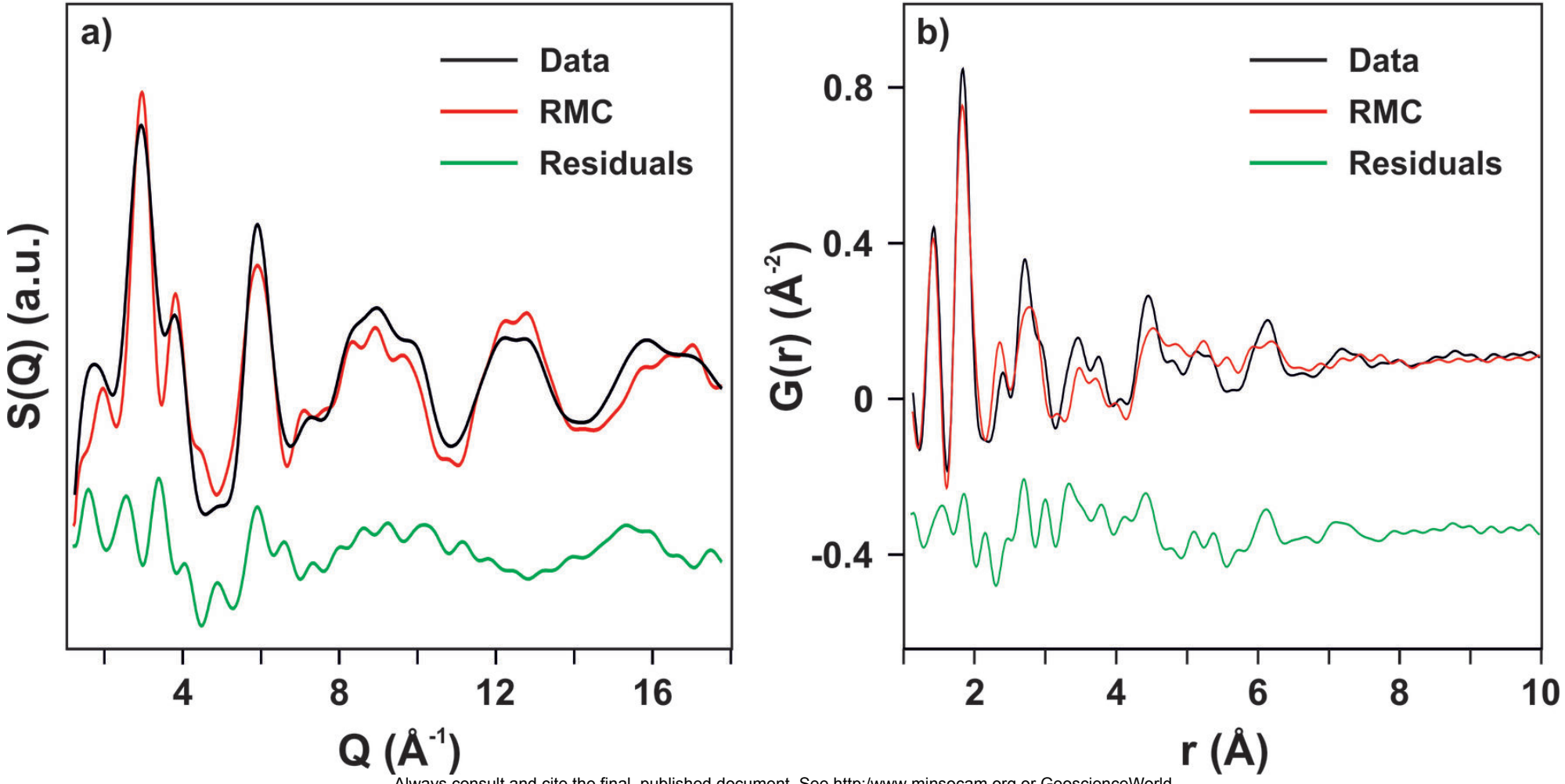

Figure 5

This is a preprint, the final version is subject to change, of the American Mineralogist (MSA)
Cite as Authors (Year) Title. American Mineralogist, in press.
(DOI will not work until issue is live.) DOI: http://dx.doi.org/10.2138/am-2017-6059

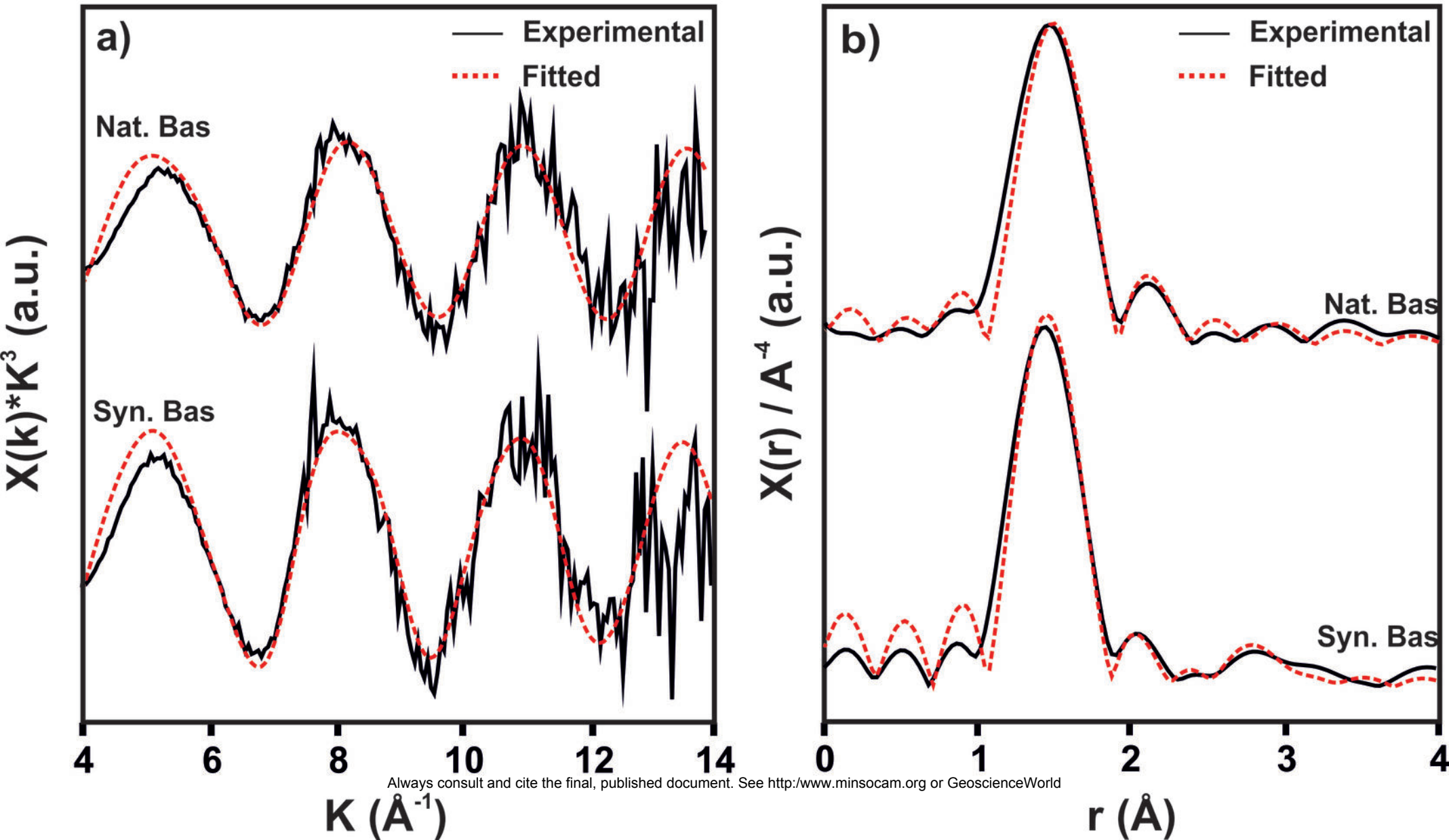

This is a preprint, the final version is subject to change, of the American Mineralogist (MSA)
Cite as Authors (Year) Title. American Mineralogist, in press.
(DOI will not work until issue is live.) DOI: http://dx.doi.org/10.2138/am-2017-6059

Table 1

Model	Path	Neighbor	N	σ^2	R	ΔE_0	V	$\Delta\chi^2$
Nat-Bas	S-O_T	One shell	5.119 ± 0.051	0.0004 ± 0.0002	1.453 ± 0.002	0.213 ± 1.320	4	16.3
Syn-Bas	S-O_O	Shell 1	4.583 ± 0.051	0.0009 ± 0.0003	1.458 ± 0.003	2.049 ± 1.201	5	17.9
	S-Al_{bi}	Shell 2	2.000 (fixed)	0.0057 ± 0.0037	3.017 ± 0.033	2.049 ± 1.201		

V: nº of variable